Comparative evaluation of DES and SAS turbulence models for incompressible flow in a Venturi tube

San Luis TOLENTINO*,[1,3], Omar GONZÁLEZ[2], Jorge MÍREZ[3]

*Corresponding author
*,[1]National Experimental Polytechnic University "AJS" Vice-Rectorate,
Puerto Ordaz (UNEXPO), Bolívar, Venezuela,
sanluist@gmail.com
[2]Faculty of Civil Engineering, National University Hermilio Valdizán (UNHEVAL),
Huánuco, Perú,
omargc17@gmail.com
[3]Group of Mathematical Modeling and Numerical Simulation (GMMNS),
Faculty of Oil, Natural Gas and Petrochemical Engineering,
Universidad Nacional de Ingeniería (UNI), Lima, Perú,
jmirez@uni.edu.pe

DOI: 10.13111/2066-8201.2022.14.2.8

Received: 29 December 2021/ Accepted: 05 May 2022/ Published: June 2022

Abstract: *Computational fluid dynamics employs the Large Eddy Simulation (LES) and Reynolds-averaged Navier-Stokes (RANS) models and combines both models to perform a hybrid RANS/LES simulation of the transient state flow field, within which there are the Detached Eddy Simulation (DES) and Scale-Adaptive Simulation (SAS) models. In the present work, the objective is to evaluate the DES and SAS turbulence models for flow (water) in a Venturi tube, for 2D computational domains. The domain was discretized for grids with quadrilateral cells, and the flow field was studied for four flow rates. The results of the pressure flow field simulations for the DES and SAS models were compared with experimental data reported in the literature, which fit the experiments. However, the DES k-ε model presented a negative pressure drop for a region of the flow adjacent to the wall, at the entrance of the throat section, the other models DES S-A, DES SST k-ω and SAS presented positive pressures. The discharge coefficients yielded values in the range of 0.94-0.951, which were lower than the experiments, for errors in the range of 1.57-2.76%.*

Key Words: *discharge coefficient, incompressible flow, DES and SAS models, pressure, RANS/LES hybrid simulation, Venturi tube*

1. INTRODUCTION

Turbulence models used in computational fluid dynamics (CFD) [1] have different mathematical structures for modeling the flow turbulence, which are used for single-phase, two-phase or three-phase flows.

They have their own characteristic response to flow velocity conditions, adverse pressure gradients, boundary layer separation and flow recirculation, for low and high Reynolds numbers [2], [3], [4].

The Reynolds number is related to the inertia forces and viscous forces, the higher the Reynolds number, the lower the boundary layer thickness [4], [5], [6].

In 1904 Prandtl introduced the boundary layer approximation, which divided the flow into two regions: an outer non-viscous flow region and an inner flow region defined as boundary layer, where the viscous force and fluid rotationality are taken into account [3], [4].

Turbulent flow is dissipative, where viscosity causes large eddies to propagate and dissipate on a smaller scale, according to the Kolmogorov length, time and velocity scale. Eddies transport mass, amount of motion and energy to other regions of the flow, thus influencing the behavior of adjacent regions, which causes them to increase their mass, amount of motion, as well as, increased heat transfer due to friction and pressure differences [2], [3], [4]. The evaluation of turbulence models for different flow field regimes allows to determine which turbulence model best fits the required conditions of flow behavior from experimental data of pressure, velocity, temperature, discharge coefficient, among others, for subsequent application to complex domains that cannot be solved with analytical equations.

The Venturi tube is used in the process industry to measure the flow rate, and is a venous contraction head loss instrument, which was invented by Clemans Herschel (1842-1930) and named after Giovanni Battista Venturi (1746-1822) for his pioneering work on flow in conic sections [4].

Experimental and numerical studies of the flow field in a Venturi tube have been addressed by different authors, for liquid, gas, and cavitation flow [7], [8], [9], [10], [11], [12], [13], [14], [15], [16], [17], [18], [19], [20], [21].

The work reported in [13] regarding numerical simulations of the pressure exerted by water flow on the walls for a type of Venturi tube, reported negative pressure drops at the inlet of the throat section, for Reynolds numbers greater than 29400; the flow was simulated with the Reynolds-Averaged Navier-Stokes (RANS) model and two turbulence models, standard $k-\varepsilon$ of Launder and Spalding [22] and standard $k-\omega$ of Wilcox [23], in COMSOL Multiphysics 4.3 which applies the Finite Element Method (FEM).

The flow (water) was simulated in steady state, without the presence of particles and water bubbles, therefore, the results of the simulations with negative magnitude pressure drops motivated to continue with the research, this time, to simulate the flow with the ANSYS-Fluent 16.2 code that applies the Finite Volume Method (FVM), for the flow conditions in transient state, in order to corroborate if for other turbulence models they present the same results of negative pressure values.

For transient state flow field simulations, Large Eddy Simulation (LES) and RANS models are combined to perform a hybrid RANS/LES simulation; within which are the hybrid turbulence models Detached Eddy Simulation (DES) and Scale-Adaptive Simulation (SAS) [24]. The equations of the DES and SAS models are modifications of base turbulence models. The $k-\varepsilon$ [22], $k-\omega$ [23], as well as the SST $k-\omega$ model of Menter [25] and S-A model of Spalart-Allmaras [26] are widely used in CFD.

For compressible flows, simulations of the flow with adverse pressure gradients and boundary layer separation are recurrently compared with experimental data, and each model has a particular behavior [27], [28]. For incompressible flows, the density is constant, so the iteration time is much shorter with respect to the variable density of compressible flows.

In the present work, the transient state incompressible flow field is simulated for 2D computational domains of a Venturi tube, for DES and SAS models, in order to determine how well the numerical results are matched with the experimental data of pressure, discharge coefficient and Reynolds number.

Section 2 presents the mathematical fundamentals, the domain, the meshing, the boundary conditions, the mesh sensitivity study, and the computational solution method. Section 3 presents the results, and Section 4 presents the conclusions.

2. MATERIALS AND METHODS

The Venturi tube used by Tolentino [13] to perform experimental tests of water flow pressure is shown in Fig. 1, who reported manometric pressures of water columns; in his work he describes the steps of how the experiment was performed. The domain, dimensions, and positions of the references from A to L shown in the same figure, were used in the domains for the flow field simulations in the present work.

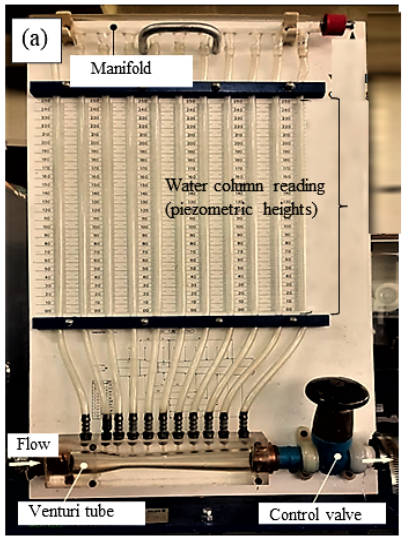

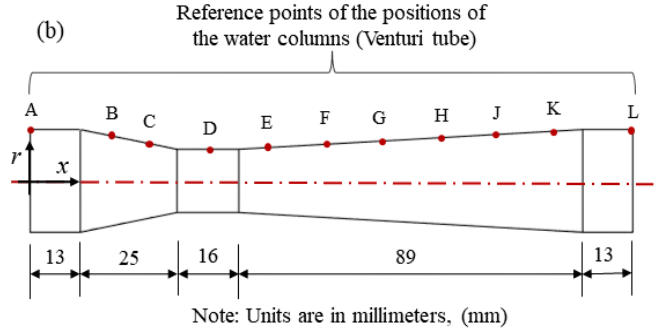

Reference:										
A	B	C	D	E	F	G	H	J	K	L
Diameter, (mm):										
26	23.2	18.4	16	16.8	18.47	20.16	21.84	23.53	25.24	26
Position, (mm):										
0	20	32	46	61	76	91	106	121	136	156

Fig. 1 – (a) Venturi tube with eleven piezometric readings of water columns. (b) Geometry, dimensions and positions of the references from A to L [13].

2.1 Mathematical fundamentals

The governing equations for the solution of the incompressible flow field in the ANSYS-Fluent 16.2 code are the conservation of mass (1) and momentum (2) equations [24], which are expressed as:

Mass conservation:

$$\frac{\partial \rho}{\partial t} + \nabla \cdot (\rho u_i) = 0 \tag{1}$$

where t is time, ρ is density and u is velocity.

Momentum:

$$\frac{\partial}{\partial t}(\rho u_i) + \nabla \cdot \left(\rho u_i u_j\right) = -\nabla p + \nabla \cdot (\bar{\bar{\tau}}) + \nabla \cdot \left(-\rho \overline{u_i' u_j'}\right) \tag{2}$$

where p is the pressure and $\bar{\bar{\tau}}$ is the stress tensor; $-\rho \overline{u_i' u_j'}$ is the Reynolds stresses, which closes to equation (2), and is a function of the turbulent viscosity, μ_t.

The stress tensor is expressed as [24]:

$$\bar{\bar{\tau}} = \mu\left[\left(\nabla u_i + \nabla u_j\right) - \frac{2}{3}\delta_{ij}\nabla \cdot u_l\right] \quad (3)$$

where μ is the molecular viscosity, l is the unit tensor, δ_{ij} is the Kronecker delta, if i and j are equal, their value is one, if they are different, then their value is zero.

For the modeling of the transient state turbulence in the present work, the hybrid turbulence models DES and SAS are used.

DES and SAS are based on one set of momentum equations throughout the RANS and LES portions of the domain. The models used are classified as, DES: DES S-A [26], [29], [30], DES Realizable $k-\varepsilon$ [31], and DES SST $k-\omega$ [32]; as well as the SST-SAS model [33], [34].

The SAS concept is based on the introduction of the von Karman length-scale into the turbulence scale equation.

The formulation of a scale-equation has been developed by Rotta (1968, 1972). This SAS source term originates from a second order derivative term in Rotta's transport equations [35].

The transport equations for the SST-SAS model as implemented in Ansys-Fluent are based on transforming Rotta's approach to $k-\omega$ (SST) [33], [34]. The $k-\varepsilon$ and $k-\omega$ models are two-equation transport models, where k is the turbulent kinetic energy, ε is the turbulent dissipation rate, and ω the specific dissipation rate.

The Spalart-Allmaras S-A model [26] is a one-equation model that solves a modeled transport equation for the kinematic viscosity of turbulent eddies. In [24] the mathematical expressions of the governing equations and the DES and SAS turbulence models are reported and detailed.

The discharge coefficient C_d [4] is determined from the following expression:

$$C_d = \frac{Q_r}{Q_t} \quad (4)$$

where, the flow rate Q_r is the real or experimental flow rate and is a known data obtained in the laboratory. Q_t is the theoretical flow rate and is expressed as:

$$Q_t = A_g\sqrt{2g\Delta h/(1-\beta^4)} \quad (5)$$

where A_g is the cross-sectional area of the throat section at reference D, g is gravity. $\Delta h = h_A - h_D$, where h_A is the gauge pressure of the water column at reference A, and h_D at the throat section, at reference D.

β is the ratio between the throat diameter (reference D) and the larger diameter (reference A) of the Venturi tube inlet, where $\beta = D_D/D_A$.

For the calculation of the flow rate Q_t, the head loss due to the effect of flow friction is not taken into account.

The Reynolds number R_e [4] is a dimensionless number, being the ratio of the inertial forces to the viscous forces:

$$R_e = \frac{\rho V D}{\mu} \quad (6)$$

where ρ is the density, V is the average velocity, D is the diameter, and μ is the dynamic viscosity.

For values less than 2300 the flow is laminar, for values greater than 4000 the flow is turbulent; for the range 2300-4000 the flow is in transition [4].

2.2 Meshing and boundary conditions

Because of the symmetry of the Venturi tube in the radial direction, it was considered to simulate the flow for 2D domains, and this is very common for symmetric geometries of bodies of revolution.

Therefore, going from a 3D to 2D domain reduces the computational cost and data processing iteration time.

The geometry of the Venturi tube for a 2D domain is shown in Fig. 2. The domain is meshed with structured mesh and quadrilateral cells; the enlarged detail shows how the quadrilateral elements are distributed on the walls and in the throat section. The same figure shows the boundary conditions.

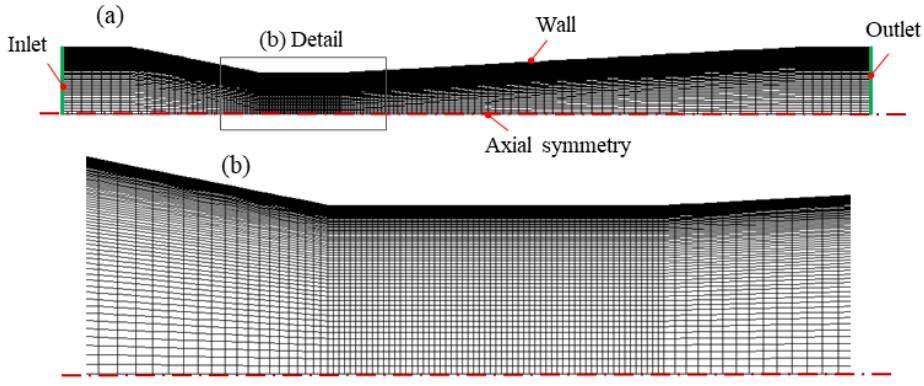

Fig. 2 – 2D domain of the Venturi tube. Structured mesh with 11480 quadrilateral elements. Cell distribution, radius for length: straight section 70x7, convergent 70x30, throat 70x60, divergent 70x60, straight section 70x7. Bias factor: 22, towards the wall. Bias factor: 5, towards throat, left side. Bias factor: 6, towards throat, right side

The experimental data [13] needed in the present work are presented in Table 1, where the gauge pressure in units of millimeters of water (mmH_2O), flow rate, mass flow, velocity and Reynolds number at reference D, and the discharge coefficient C_d are given. It should be noted that the velocity in the throat section was calculated with the experimental flow rate, and with the experimental and theoretical flow rate the discharge coefficient was calculated with Equation (4).

Table 1 – Parameters for four experimental flow rate readings [13]

Exp.	Pressure ΔP_{A-L} (mmH_2O)	Flow Rate 10^4 (m^3/s)	Mass flow rate (kg/s)	Velocity (m/s) Ref. D	Reynolds number Ref. D	Discharge coefficient C_d
2	14.5	2.583	0.257551	1.28468	22489	0.955
3	18	2.991	0.298233	1.48760	26041	0.971
4	23	3.382	0.337120	1.68206	29445	0.977
5	26.5	3.704	0.369326	1.84221	32249	0.979

The gauge pressures at each reference, from A to L, are used to compare the numerical results of the turbulence models.

The pressure differences (ΔP_{A-L}), at the inlet, A, and outlet, L, of the water flow in the Venturi tube, were taken as references in the simulations to identify for each experiment: Exp. 2 ($\Delta P_{A-L} = 14.5\ mmH_2O$), Exp. 3 ($\Delta P_{A-L} = 18\ mmH_2O$), Exp. 4 ($\Delta P_{A-L} = 23\ mmH_2O$) and Exp. 5 ($\Delta P_{A-L} = 26.5\ mmH_2O$), respectively. The same values of the water temperature at 24°C were taken into account, being the density $\rho = 997.1015\ kg/m^3$, and the dynamic viscosity $\mu = 9.1135x10^{-4}\ Pa \cdot s$.

The boundary conditions for the flow at the inlet and outlet of the Venturi tube are shown in Table 2.

The values of the pressures are the same as those reported by Tolentino [13], and when entering the data into the ANSYS-Fluent code they should be entered in Pascal units. The domain wall was considered adiabatic.

In axial symmetry, in the x-axis in the radial direction, the flow velocity is zero; at the wall also the velocity is zero due to the no-slip condition.

Table 2 – Boundary conditions at the inlet and outlet of the Venturi tube

		ΔP_{A-L} (mmH_2O)			
		14.5	18	23	26.5
Inlet:	Velocity (m/s)	0.4865	0.56335	0.63699	0.69764
Inlet:	Pressure (mmH_2O)	170	179	190	199.5
Outlet:	Pressure (mmH_2O)	155.5	161	167	173

For numerical convergence, a sensitivity study of the mesh with quadrilateral cells was performed in the ANSYS-Meshing platform.

The domain was refined three times: a first meshing for 9840 elements, a second meshing for 10660 elements and a third meshing for 11480 elements.

Pressure loading for $\Delta P_{A-L} = 14.5\ mmH_2O$ and the DES S-A turbulence model were applied and compared with experimental data [13].

The numerical results yielded results adjusted to the experimental ones (Fig. 3a), as well as, yielded lower values of $y^+ < 1$, except for the regions at the entrance and final section of the convergent joining with the throat, which obtained $y^+ < 1.45$ (Fig. 3b). The third meshed domain with 11480 elements is the most satisfactory, so it was taken into consideration in the simulations of the flow field of the present work.

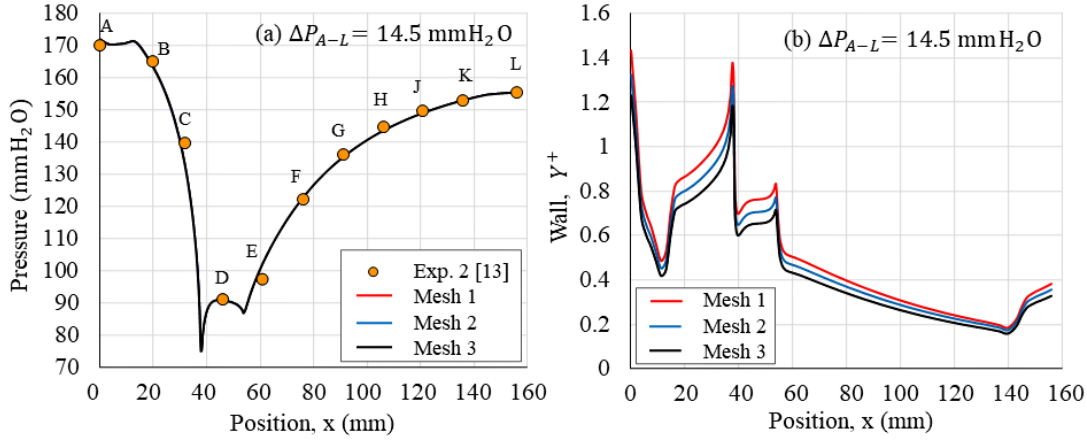

Fig. 3 – Numerical simulations with the DES S-A turbulence model, for three refined grids. (a) Comparison of gauge pressure profiles at the Venturi tube wall with experimental data [13]. (b) Profiles y^+ evaluated at the wall

2.3 Computational solution method

In ANSYS-Fluent 16.2 the following considerations were taken into account: in Solver, Type: pressure-based; Velocity formulation: absolute; Time: transient; 2D space: axisymmetric. In viscous model, Model: DES, y RANS model: S-A, Realizable $k-\varepsilon$, SST $k-\omega$. Also, the Model: SAS.

In the solution methods, in pressure-velocity coupling, scheme: SIMPLE. In spatial discretization, Gradient: Least Squares Cell Based; pressure: Second Order; Momentum: Bounden Central Differencing; Modified turbulent viscosity: Second Order Upwind.

In transient formulation: Second Order Implicit. For the residual monitor, a fixed value of 1×10^{-7} was determined. The hybrid initialization method was applied. 2000 iterations were performed to obtain the flow field results for pressure and velocity.

A computer with the following characteristics was used for data processing: Dell CPU, Optiplex 7010 model, i5 3470, four 3.2 GHz processors and 8 GB of RAM memory.

3. RESULTS AND DISCUSSIONS

Flow field simulations for pressure are shown in Fig. 4 for $\Delta P_{A-L} = 14.5\ \mathrm{mmH_2O}$, $\Delta P_{A-L} = 18\ \mathrm{mmH_2O}$, $\Delta P_{A-L} = 23\ \mathrm{mmH_2O}$ and $\Delta P_{A-L} = 26.5\ \mathrm{mmH_2O}$.

The pressure distributions are similar between the DES and SAS models, where the magnitude differences in the flow field are observed.

The pressure contour lines in the central region of the flow are different between the turbulence models, which have a defined behavior in the direction of the flow; and this is a consequence of the structures of the mathematical models to model turbulence, for each specific, such as for DES S-A, DES $k-\varepsilon$, DES SST $k-\omega$ and SAS.

In the throat section, pressure drops and increased flow velocity are present. For $\Delta P_{A-L} = 26.5\ \mathrm{mmH_2O}$, the DES $k-\varepsilon$ model presents a negative magnitude of $-0.16\ \mathrm{mmH_2O}$ (Fig. 4d) for the flow region adjacent to the wall between the converging section and the throat, indicating that the flow there presents cavitation. Similar results with negative values of the pressure in that indicated region below $-20\ \mathrm{mmH_2O}$ were reported in [13], where the steady-state flow field was simulated with the COMSOL Multiphysics code and Solver PARDISO, for the standard $k-\varepsilon$ [22] and standard $k-\omega$ [23] turbulence models.

Although the flow during the experiments [13] did not present bubbles, what the numerical results of the present work indicate in transient state is that the apex at the throat inlet influences abrupt pressure drops, when the flow velocity increases in the throat section.

Therefore, it should be taken into account for comparison with other steady-state turbulence models if they present similar results, for different types of meshing and for algorithm schemes other than SIMPLE, in order to have a wider scope in the analysis of the flow behavior in the throat section.

The flow pressures at the walls and at the axial symmetry of the Venturi tube are shown in Fig. 5, and define a similar pattern of behavior, although the magnitudes of the pressures at the inlet and outlet of the Venturi tube undergo changes.

The lowest pressure drop of the flow in the wall occurs at the junction between the convergent section and the throat, and the other pressure drop with lower intensity occurs for the other end of the throat, thus, the throat section is a critical region for the flow.

The pressures in the axial symmetry have a similar behavior. The wall pressure and axial symmetry pressure profiles of the DES and SAS models border and intercept with the experimental pressure data [13].

It is observed that the DES S-A and DES $k-\varepsilon$ models fit best with the experimental data. While the DES SST $k-\omega$ and SAS models diverge at the Venturi tube inlet, in reference A, however, they fit with the experimental pressure data better at the throat section, in reference D. In the divergent, the pressure profiles evaluated at wall and axial symmetry follow the same pattern throughout the experimental data, showing that the pressures tend to behave perpendicular to the flow direction.

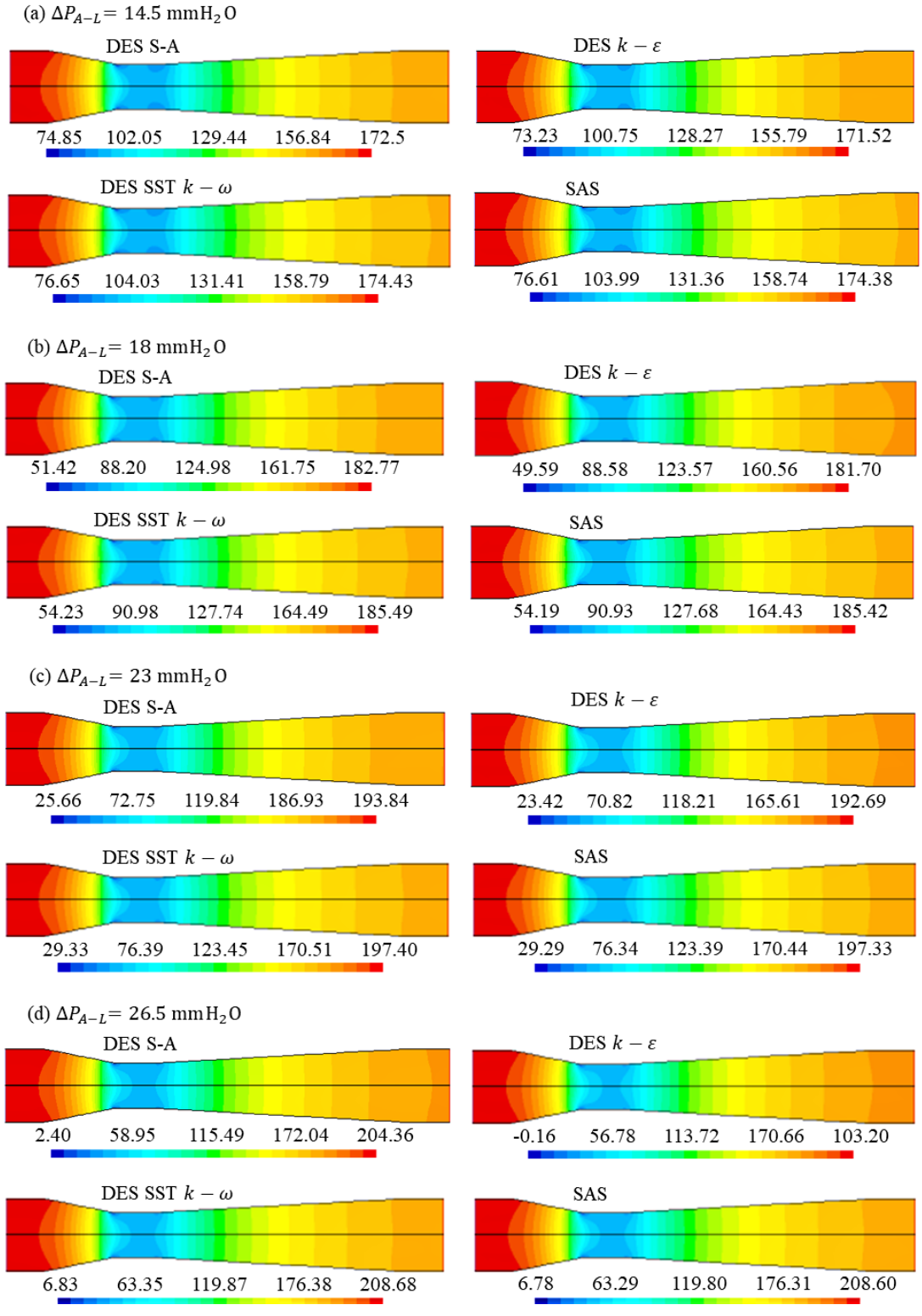

Fig. 4 – Pressure field (mmH$_2$O) for DES and SAS turbulence models

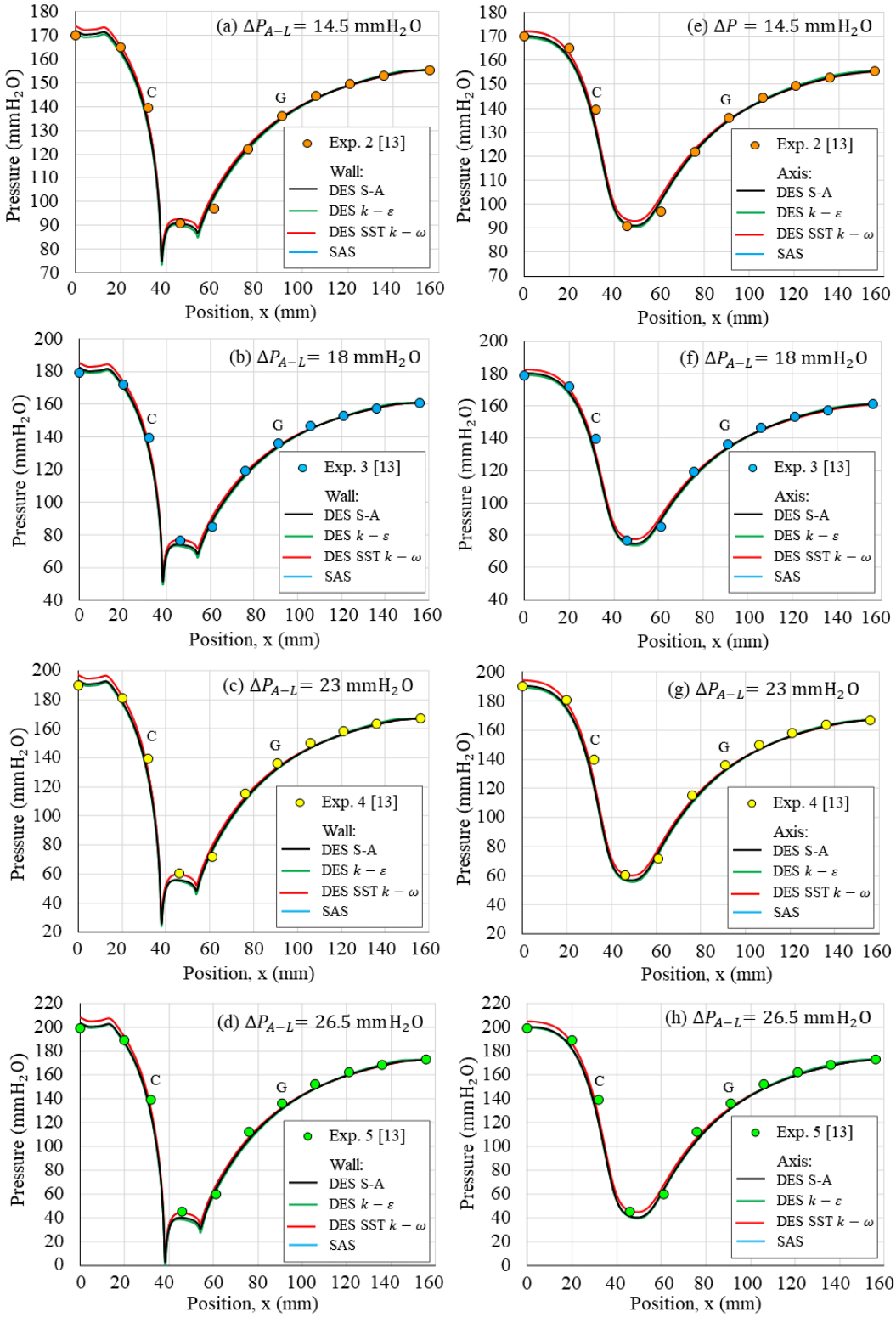

Fig. 5 – Pressure profiles of DES and SAS turbulence models compared with experimental data [13]. (a-d) Pressure patterns at the wall. (e-h) Pressure patterns in axial symmetry

In references C and G the profiles are intercepted, there the magnitudes of the pressures (Fig. 5) remain constant, however, there the velocities are not constant. It should be noted that the pressure behavior of the experimental data in references C and G [13], is because the flow rate is controlled by the valve at the inlet of the Venturi tube, which is not shown in Fig. 1, and the valve at the outlet of the Venturi tube the opening remains unchanged. The air trapped in the manifold keeps the water columns in equilibrium in the absence of atmospheric pressure. Similar results of the curves of the numerical simulations, for references C and G were reported by Tolentino [13], therefore, the numerical results for domains discretized by FEM and FVM are congruent.

The discharge coefficients and Reynolds numbers from the simulations for the DES and SAS models are compared with experimental data, which are shown in Fig. 6. The discharge coefficient and Reynolds number calculated based on the mass flow in the throat section at reference D are shown in Fig. 7a and 7e, and those based on the average velocity are shown in Fig. 7b and 7f.

The discharge coefficients and Reynolds number calculated with equations (4) and (6), with the local average pressure in references A and D are shown in Fig. 6c and 6g; for the local wall pressure, in references A and D, they are shown in Fig. 7d and 7h.

The numerical results of the discharge coefficients that fit best with the experimental data (Table 1, C_d: $0.955 - 0.978$) are for the average pressures (Fig. 6c), which are in the range of C_d: $0.946 - 0.957$, and for percentage errors in the range of $0.85 - 2.19\%$. While the discharge coefficients calculated for the wall pressures (Fig. 6d) have smaller magnitudes, and are in the range of C_d: $0.94 - 0.951$, for percentage errors they are in the range of $1.57 - 2.76\%$.

From these two results, the numerical solution to be taken into account is for the discharge coefficients calculated for the wall pressures (Fig. 6d), since for the experiments, the discharge coefficients were calculated with the gauge pressures (water columns, mmH_2O), which are lower than those reported by the experiments (Table 1). The results of the DES S-A and DES $k - \varepsilon$ models are closer to the experimental data, and the DES SST $k - \omega$ and SAS models slightly away.

With respect to the discharge coefficients shown in Fig. 6a, the values are around 1, and for Fig. 6b they are greater than 1. In both cases, the calculation was performed for the mass flow and average velocity in the throat section, at reference D, and that is why the results are different with respect to the calculation of the theoretical flow that is determined by pressure differences (Fig. 6c and 6d) and without considering the losses due to flow friction. For both cases, the behavior of the Reynolds number is shown, where, in Fig. 6e the Reynolds number of the numerical simulation is superimposed over the experimental Reynolds number, and Fig. 6f shows that it is below the experimental data. In Fig. 6g and 6h, the Reynolds numbers are higher than the experimental data, which were calculated with the theoretical flow velocities that take into account the pressure differences. The Reynolds number presented percentage errors in the range of $4.5 - 5.6\%$ for the average pressure (Fig. 6g) and $5.1 - 6.3\%$ for the local pressure (Fig. 6h).

The pressure and velocity profiles in the radial direction in the throat section at reference D are shown in Fig. 7a-d. The pattern of the pressure profiles is shown, where the pressure is higher in the central region, and their behavior are similar to each other as the flow rate increases. The one with the lowest pressure is the DES $k - \varepsilon$ model, followed by the DES S-A model, the other two DES SST $k - \omega$ and SAS models are together, and the one with the highest pressure is the DES SST $k - \omega$ model.

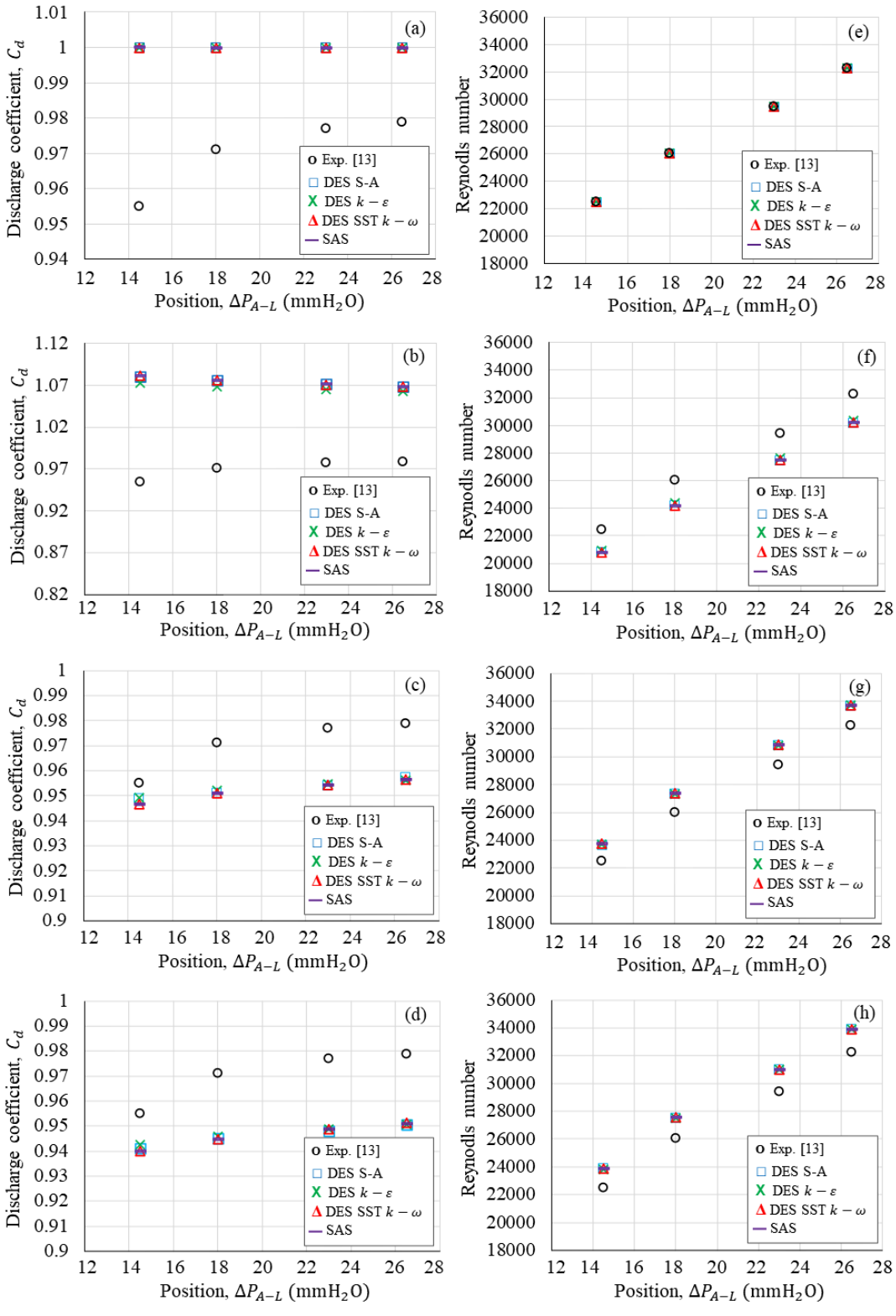

Fig. 6 – Comparison of discharge coefficients and Reynolds number with experimental data (Table 1)

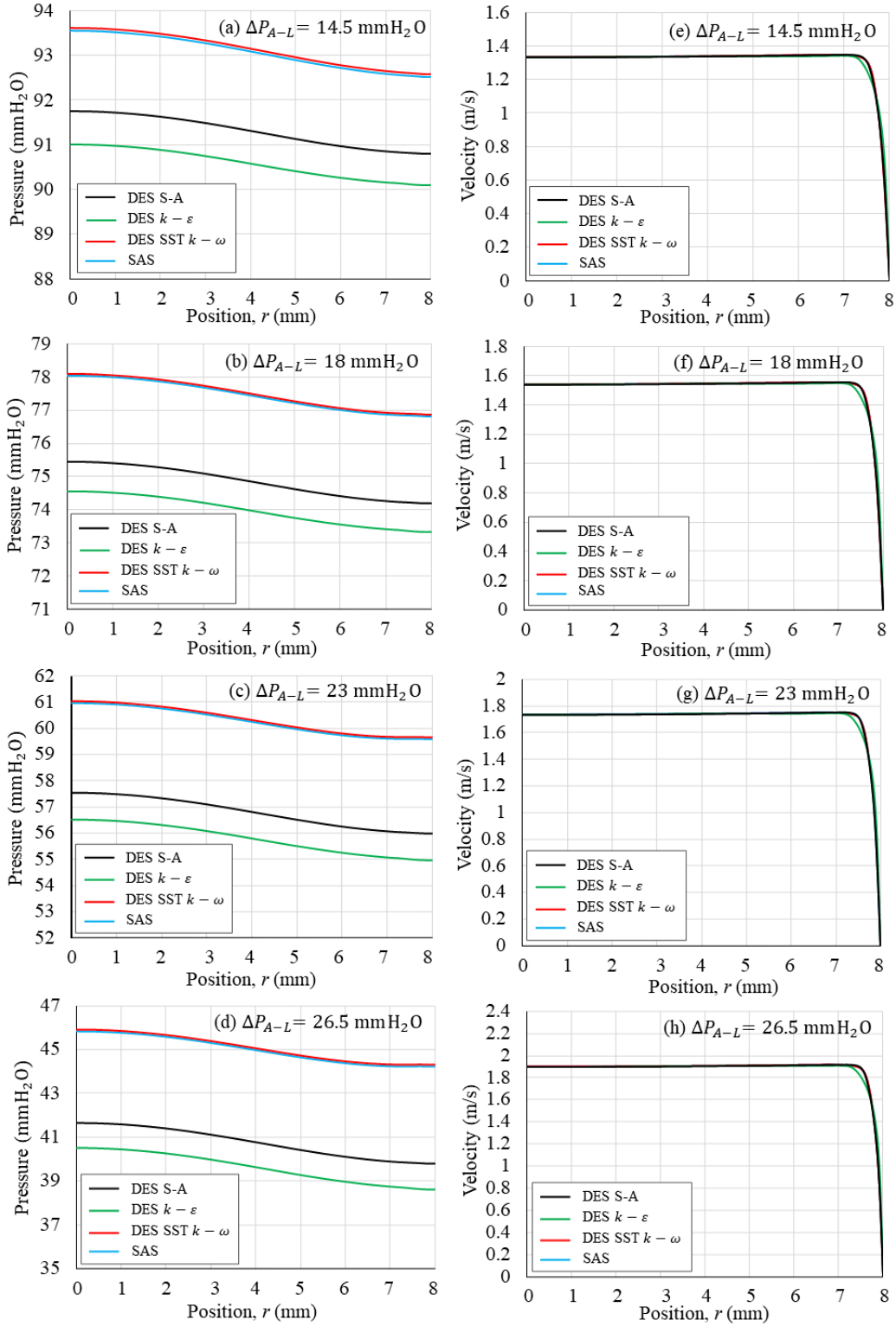

Fig. 7 – Pressure (mmH$_2$O) and velocity (m/s) flow patterns in the throat section at reference D for the DES and SAS turbulence models

The flow velocity behavior pattern due to flow turbulence and boundary layer are shown in Fig. 7e-h, where the velocity tends to be normal in the axial direction, and the flow region adjacent to the wall tends to curve to meet the rest by the no-slip condition. At the upper right end where a corner is formed, at the estimated position $r = 7.5$ mm, the DES $k - \varepsilon$ model of the velocity profiles is less pronounced, the other models: DES S-A, DES SST $k - \omega$ and SAS are slightly overlapping each other; therefore, in the region adjacent to the wall, the DES and SAS models present different velocity patterns.

4. CONCLUSIONS

The DES and SAS turbulence models were simulated in 2D domains with structured mesh with quadrilateral cells, which present different pressure and velocity behaviors in the flow field.

The profiles of the DES and SAS turbulence models fit the experimental pressure data. The percentage errors of the numerical results of the discharge coefficients for the average pressure (Fig. 6c) are in the range of $0.85 - 2.19\%$, for the local wall pressure (Fig. 6d) in the range of $1.57 - 2.76\%$.

The percentage errors of the numerical results of the discharge coefficients for the average pressure are in the range of $0.85 - 2.19\%$ for the local wall pressure in the range of $1.57 - 2.76\%$. The percentage errors for the Reynolds number are in the range of $4.5 - 5.6\%$ for the average pressure, and $5.1 - 6.3\%$ for the local pressure.

In the throat section, at the throat entrance, the only turbulence model that presents negative pressure is the DES $k - \varepsilon$ model for Reynolds greater than 32000, whereas, the DES S-A, DES SST $k - \omega$ and SAS models present positive pressures.

In future work, it is planned to evaluate different turbulence models for steady state flow for 2D and 3D domains of the Venturi tube used in the present work, applying different computational codes, in order to compare the numerical results with the experimental pressure data reported in [13].

REFERENCES

[1] J. H. Ferziger, M. Perić and R. L Street, *Computational methods for fluid dynamics,* Germany, Springer Verlag, 4th ed., 2019.

[2] T. V. Karman, The fundamentals of the statistical theory of turbulence, *Journal of the Aeronautical Sciences*, vol. **4**, no. 4, pp. 131–138, 1937, https://doi.org/10.2514/8.350

[3] H. Schlichting and K. Gersten, *Boundary-layer theory*, Berlin Heidelberg, Germany, Springer Verlag, 9th ed., 2017.

[4] Y. A. Cengel and J. M. Cimbala, *Fluids Mechanics: Fundamentals and applications*, USA, McGraw-Hill, 4th ed., 2020.

[5] O. Reynolds, An experimental investigation of the circumstances which determine whether the motion of water shall be direct or sinuous, and of the law of resistance in parallel channels author(s): Osborne Reynolds, *Philosophical Transactions of the Royal Society of London*, vol. **174**, pp. 935–982, 1883.

[6] N. Rott, Note on the history of the Reynolds number, *Annual Review of Fluid Mechanics*, vol. **22**, no. 1, pp. 1–12, 1990, https: //doi.org/10.1146/annurev.fl.22.010190.000245

[7] D. Lindley, An experimental investigation of the flow in a classical venturi meter, *Proc. of the Instit. of Mech. Engin.*, vol. **184**, no. 1, pp. 133–160, 1969, https://doi.org/10.1243/PIME_ PROC_1969_184_015_02

[8] M. J. Reader-Harris, W. C. Brunton, J. J. Gibson, D. Hodges and I. G. Nicholson, Discharge coefficients of Venturi tubes with standard and non-standard convergent angles, *Flow Measurement and Instrumentation*, vol. **12**, no. 2, pp. 135–145, 2001, https://doi.org/10.1016/S0955-5986(01)00007-3

[9] K. Perumal and J. Krishnan, A CFD study of the effect of venturi geometry on high pressure wet gas metering, *International Journal of Oil Gas and Coal Technology*, vol. **6**, no. 5, pp. 549 – 566, 2013, Available at https://www.inderscienceonline.com/doi/abs/10.1504/IJOGCT.2013.056101

[10] A Tukimin, M. Zuber and K. A. Ahmad, *CFD analysis of flow through Venturi tube and its discharge coefficient*, in IOP Conf. Series: Materials Science and Engineering vol. **152**, 012062, 2016, Available at https://iopscience.iop.org/article/10.1088/1757-899X/152/1/012062

[11] S. Salomo, Estimation optimal value of discharge coefficient in a Venturi tubes, *IOP Conf. Series: Journal of Physics: Conf. Series* 1230, 012087, 2019. Available at https://iopscience.iop.org/article/10.1088/1742-6596/1230/1/012087

[12] H. Wu, Y. Xu, J. Wang, T. Zhang and H. Wang, Study on the similarity of wet gas pressure drop in long-throat Venturi, *Flow Measurement and Instrumentation,* vol **68**, 101580, pp. 1-13, 2019, https://doi.org/10.1016/j.flowmeasinst.2019.101580

[13] S. L. Tolentino, Experimental and numerical study of the pressure of the water flow in a venturi tube, *Ingenius*, no. 23, pp. 9-22, 2020. https://doi.org/10.17163/ings.n23.2020.01

[14] H. Denghui and B. Bofeng, A new correlation for wet gas flow rate measurement with Venturi meter based on two-phase mass flow coefficient, *Measurement*, vol. **58**, pp. 61-67, 2014, https://doi.org/10.1016/j.measurement.2014.08.014

[15] S. Brinkhorst, E. V. Lavante and G. Wendt (2015), Numerical investigation of cavitating Herschel Venturi-Tubes applied to liquid flow metering. *Flow Measurement and Instrumentation*, vol. **43**, pp. 23–33, 2015, https://doi.org/10.1016/j.flowmeasinst.2015.03.004

[16] L. Y. Wang, B. Ji, H. Y. Cheng, J. Wang and X. Long, One-dimensional/three-dimensional analysis of transient cavitating flow in a venturi tube with special emphasis on cavitation excited pressure fluctuation prediction, *Sci China Tech Sci*, pp. 1-11, 62, 2019, https://doi.org/10.1007/s11431-019-9556-6

[17] X. Zhanga, D. Wangc , R. Liaoa, H. Zhaoa and B. Shia, Study of mechanical choked Venturi nozzles used for liquid flow controlling, *Flow Measurement and Instrumentation*, vol **65**, pp. 158-165, 2019, https://doi.org/10.1016/j.flowmeasinst.2018.12.001

[18] X. Liu, L. Lao and G. Falcone, A comprehensive assessment of correlations for two-phase flow through Venturi tubes, *Journal of Natural Gas Science and Engineering*, vol. **78**, 2020, https://doi.org/10.1016/j.jngse.2020.103323

[19] J. Zhu, S. Wang and X. Zhang, Influences of thermal effects on cavitation dynamics in liquid nitrogen through venturi tube, *Phys. Fluids*, vol.**32**, no. 1, pp. 012105 1-12, 2020, https://doi.org/10.1063/1.5132591

[20] A. Razali, M. Baghdad and A. Ouadha, *CFD-Exergy analysis of the flow in a small-sized Venturi*, International Conference on Materials & Energy (ICOME'17 and ICOME'18), vol. **307**, pp. 1-8, 2020, Available at https://doi.org/10.1051/matecconf/202030701037

[21] J. Xiao, Z. Liang, X. Liu, Z. Zhao and X. Xie, Design Optimization Analysis of Venturi Tube for Medium Conveying in Strengthen Grinding Process, *Engineering*, vol. **13**, no. 8, pp. 431-447, 2021, https://doi.org/10.4236/eng.2021.138031

[22] B. E. Launder and D. B. Spalding, *Lectures in mathematical models of turbulence*, A. P. London, New York, Ed., 1972.

[23] D. C. Wilcox, Reassessment of the scale-determining equation for advanced turbulence models, *AIAA Journal*, vol. **26**, no. 11, pp. 1299–1310, 1988. https://doi.org/10.2514/3.10041

[24] ANSYS. *Ansys Fluent Theory guide* v.14, November 2011, Available at https://kargosha.com/file/attach/201705/2812.pdf

[25] F. R. Menter, Two equation eddy-viscosity turbulence models for engineering applications, *AIAA Journal*, vol. **32**, no. 8, pp. 1598–1605, 1994. https://doi.org/10.2514/3.12149

[26] P. Spalart and S. Allmaras, *A one-equation turbulence model for aerodynamic flows*, Technical Report AIAA-92-0439, American Institute of Aeronautics and Astronautics, 1992.

[27] S. L. Tolentino, Evaluation of turbulence models for the air flow in a planar nozzle, *Ingenius*, no. 22, pp. 25–37, 2019, https://doi.org/10.17163/ings.n22.2019.03

[28] S. L. Tolentino, Evaluation of Turbulence Models for the Air Flow in a Transonic Diffuser, *Revista Politécnica,* vol. **45**, no. 1, pp. 25-38, 2020. https://doi.org/10.33333/rp.vol45n1.03

[29] M. Shur, P. R. Spalart, M. Strelets, and A. Travin, *Detached-Eddy Simulation of an Airfoil at High Angle of Attack*, In 4th Int. Symposium on Eng. Turb. Modeling and Experiments, Corsica, France. May 1999

[30] P. R. Spalart, S. Deck, M. L. Shur, K. D. Squires, M. K. Strelets, and A. Travin, A new version of detachededdy simulation, resistant to ambiguous grid densities, *Theor. and Comp. Fluid Dynamics*, **20**, 181–195, 2006.

[31] T.-H. Shih, W. W. Liou, A. Shabbir, Z. Yang, and J. Zhu, A New $k-\varepsilon$ Eddy-Viscosity Model for High Reynolds Number Turbulent Flows - Model Development and Validation, *Computers Fluids*, **24**(3), 227–238, 1995.

[32] F. R. Menter, M. Kuntz, and R. Langtry, *Ten Years of Experience with the SST Turbulence Model*, In K. Hanjalic, Y. Nagano, and M. Tummers, editorsTurbulence, Heat and Mass Transfer. 4, Begell House Inc. 625–632. 2003.

[33] Y. Egorov and F. R. Menter, *Development and application of SST-SAS turbulence model in the DESIDER project*, in Advances in Hybrid RANS-LES Modelling, S. H. Peng and W. Haase, Eds., vol. **97** of Notes on Numerical Fluid Mechanics and Multidisciplinary Design, pp. 261–270, Springer, Berlin, Heidelberg, 2008.

[34] F. Menter and Y. Egorov. The Scale-Adaptive Simulation Method for Unsteady Turbulent Flow Predictions. Part 1: Theory and Model Description, *Journal Flow Turbulence and Combustion*, **85**, 113–138, 2010.

[35] F. R. Menter and Y. Egorov, *Re-visiting the Turbulent Scale Equation*, Proc. IUTAM Symp. One Hundred Years of Boundary Layer Research, Göttingen, Springer, 2004.